Neuron, Vol. 42, 703–716, June 10, 2004, Copyright ©2004 by Cell Press

Intraflagellar Transport Genes Are Essential for Differentiation and Survival of Vertebrate Sensory Neurons

Motokazu Tsujikawa and Jarema Malicki*
Department of Ophthalmology
Harvard Medical School
243 Charles Street
Boston, Massachusetts 02110

Summary

Cilia play diverse roles in vertebrate and invertebrate sensory neurons. We show that a mutation of the zebrafish *oval* (*ovl*) locus affects a component of the ciliary transport (IFT) mechanism, the IFT88 polypeptide. In mutant retina, cilia are generated but not maintained, producing the absence of photoreceptor outer segments. A loss of cilia also occurs in auditory hair cells and olfactory sensory neurons. In all three sense organs, cilia defects are followed by degeneration of sensory cells. Similar phenotypes are induced by the absence of the IFT complex B polypeptides, *ift52* and *ift57*, but not by the loss of complex A protein, *ift140*. The degeneration of mutant photoreceptor cells is caused, at least partially, by the ectopic accumulation of opsins. These studies reveal an essential role for IFT genes in vertebrate sensory neurons and implicate the molecular components of intraflagellar transport in degenerative disorders of these cells.

Introduction

Eukaryotic cilia and flagella are highly conserved organelles that project from the surfaces of many cells. Sensory neurons of vertebrates and invertebrates display well-developed cilia that in some cases appear necessary for the formation of specialized detector structures, such as photoreceptor outer segments in the vertebrate eye. Photoreceptor cells in the eye, hair cells of the auditory system, and olfactory sensory neurons all feature prominent cilia. The importance of cilia in photoreceptor cells is particularly obvious. The vertebrate photoreceptor cell utilizes as many as 10^9 visual pigment molecules, which are synthesized in the cell body and from there transported into the outer segment along the photoreceptor connecting cilium (Pugh and Lamb, 2000). Although in a smaller quantity, olfactory cilia also contain olfactory receptors and other elements of signal transduction cascade (Leinders-Zufall et al., 1997; reviewed in Zufall and Leinders-Zufall, 2000). The role of hair cell cilia, kinocilia, in auditory perception is less clear (Hudspeth and Jacobs, 1979). As cilia are devoid of protein synthesis, the formation of cilliary axoneme and structures that derive from cilia, such as photoreceptor outer segments, requires the translocation of proteins from the cytoplasm along the cilium. This movement is thought to be mediated by intraflagellar transport (IFT) particles (reviewed in Rosenbaum et al., 1999; Rosenbaum and Witman, 2002). Proteins required in cilia are assembled into IFT particles at the cilium base, where they also associate with kinesin, a motor protein complex that mediates their anterograde transport along the axoneme.

The IFT particle has been studied in diverse species. Experiments in *Chlamydomonas* identified at least 17 proteins that contribute to its structure. Based on biochemical studies, these polypeptides are believed to assemble into two complexes, named A and B (Cole et al., 1998). Interestingly, the same genes that form the *Chlamydomonas* IFT particle have been identified independently in *C. elegans* during genetic screens for defects in chemosensory neurons, and they function in cilia of these cells (Perkins et al., 1986). The protein products of the *C. elegans osm-1, osm-5, osm-6, che-13, che-11*, and *daf-10* are homologs of *Chlamydomonas IFT172, IFT88, IF52, IFT57, IFT140*, and *IFT122*, respectively (reviewed in Rosenbaum and Witman, 2002). IFT particle mutants have also been identified in the mouse and *Drosophila* (Kernan et al., 1994; Moyer et al., 1994). The vertebrate IFT mutations are mainly associated with deformities in early embryogenesis and kidney development, while invertebrate genetic defects mostly cause sensory neuron abnormalities that result in a variety of aberrant behaviors (Han et al., 2003; Haycraft et al., 2001; Murcia et al., 2000; Pazour et al., 2000; Qin et al., 2001). The function of IFT genes in vertebrate neurons, however, has remained largely obscure.

Mutations in the zebrafish *oval* (*ovl*) locus cause photoreceptor loss and kidney cysts (Doerre and Malicki, 2002). We present evidence that *ovl* encodes a homolog of the intraflagellar particle component, *IFT88*. *ovl* function is necessary for the maintenance but not for the initial assembly of sensory cell cilia. Consistent with this observation, photoreceptor outer segments are absent in *ovl* null animals. Unexpectedly, in the absence of *ovl* function, sensory cells degenerate in the visual, auditory, and olfactory systems. To further investigate the role of intraflagellar transport in sensory neurons, we identified zebrafish homologs of other IFT particle components: *ift52*, *ift57*, and *ift140*. Knockdown experiments indicate that similar to *ovl*/*ift88*, other complex B proteins are also essential for cilia maintenance and sensory neuron survival: cilia are resorbed in *ift52* and *ift57* knockdown animals, and subsequently all types of sensory cells that we have investigated so far degenerate. *ift140*, a member of the IFT complex A, produces a much weaker phenotype. These studies demonstrate the essential role of IFT genes in the differentiation and the survival of vertebrate sensory neurons.

Results

Molecular Characterization of the *oval* Locus

To determine the molecular structure of the *oval* locus, we first mapped it to the centromeric region of linkage group 9 (LG9) using half-tetrad analysis (Streisinger et al., 1986). Subsequent high-resolution linkage analysis using an F2 mapping panel showed 13 recombination

*Correspondence: jarema_malicki@meei.harvard.edu

Figure 1. The Zebrafish *ovl* Gene

(A) Chromosomal position of the *ovl* locus.

(B) The *ovl* sequence is homologous to the mouse and human *Tg737*. Comparison using clustalW (Thompson et al., 1994). Asterisk indicates complete conservation, colon indicates highly conserved substitution, and period indicates semiconservative substitutions (below the alignment).

(C) The *ovl* protein sequence contains 9 TPR repeats (boxes). *ovl*^{tz288b} mutation is indicated (arrow).

(D) Exon/intron structure of the *ovl* transcript. The position of the *ovl*^{tz288b} mutation and of the intragenic *Bcl* I polymorphism, MTJM10RFLP, are indicated. As we have not determined the transcription initiation site, additional exons may be present in the 5′ region.

events in 1400 meioses between the polymorphic marker z17326 and the *ovl* locus. These experiments confined *ovl* to a ~3.5 cM interval between the markers z5080 and z17326 (Figure 1A) and allowed us to test candidate expressed sequence tags (ESTs) that map to this interval. Using an intragenic RFLP polymorphism, MTJM10RFLP, in the sequence of the EST *fb37b11*, we did not detect any recombination events between *fb37b11* and *ovl* in 1400 meioses.

The EST clone *fb37b11* has homology to the 3′ region of the mouse and human *IFT88* gene (also known as *Tg737* and *polaris*). Because *IFT88*-deficient mice show a polycystic kidney phenotype accompanied by retinal defects, *IFT88* seemed to be a strong candidate for the *ovl* gene. To identify its full-length ORF, we cloned the *ift88* cDNA using RT-PCR. The zebrafish *ift88* sequence encodes an open reading frame of 824 amino acids, consists of at least 26 exons, and spans approximately 17 kb on chromosome 9 (Figures 1B–1D). Sequence comparisons reveal a high degree of homology between the zebrafish and the mouse (73% identity, 85% similarity) as well as the zebrafish and man (71% identity, 83% similarity). Similar to other vertebrate genes, the zebrafish Ift88 polypeptide contains 9 TPR repeats (Meyer et al., 1996; Schrick et al., 1995). To identify the molecular defects responsible for the *ovl*^{tz288b} phenotype, we sequenced the *ovl* gene from wild-type and mutant animals. This analysis revealed 11 single nucleotide alternations between homozygous *ovl* map cross embryos and their wild-type siblings. Eight of them are silent substitutions, and two produce single amino acid changes, C220Y and G759S, that are also observed in the wild-type AB/AB background. One mutation, the nt779T→A transition in exon 11, is not observed in any wild-type strain and results in a premature stop codon, L260X (Figures 2A and 2B). In RT-PCR analysis, the *ovl*^{tz288b} mutant allele displays a shortened PCR fragment in addition to the expected one (Figure 2C, bottom left inset). Based on this result, we hypothesized that in some *ovl*^{tz288b} transcripts, the premature stop codon results in exon skipping. Sequence analysis of mutant cDNA revealed that this is indeed the case: exon11 is missing in the shortened form of the *ovl*^{tz288b} transcript, resulting in a frameshift and a premature termination codon within exon 12 (Figure 2C). Both the premature termination codon at position 260 and the deletion of exon 11 produce truncations of the Ovl polypeptide in the area of the second TPR repeat. These results strongly suggest that the nt779T→A transition is responsible for the *ovl* phenotype.

To confirm that *ovl* encodes zebrafish *ift88*, we injected anti-*ift88* morpholinos into AB background embryos. Both 5′UTR-directed and splice site-directed morpholinos reproduce the *ovl* morphological phenotype (Figure 2G, Table 1). At 3 dpf, ~90% of ATG and 40% of SP morpholino-injected fish display abnormal body curvature that characterizes the *ovl* mutant phenotype (Figure 2G). As judged by RT-PCR, the SP morpholino blocks the *ovl* mRNA splicing at least until 48 hpf (Figures 2L and 2M). Splicing is also nearly completely blocked at 72 hpf in embryos that show an abnormally curved body axis. In embryos that do not display a curved body axis, the inhibition of splicing appears incomplete (Figure 2L, lane 4). Similar to the *ovl* phenotype (see below), morpholino-treated fish lack olfactory cilia at 72 hpf (Table 1, Figure 2J). In contrast, these cilia are normal in control morpholino-injected animals (Figure 2H). To provide further evidence that a mutation in the zebrafish *ift88* gene is responsible for the *ovl* phenotype, we rescued the *ovl* defect by injecting mRNA encoding the complete *ift88* coding sequence. To demonstrate

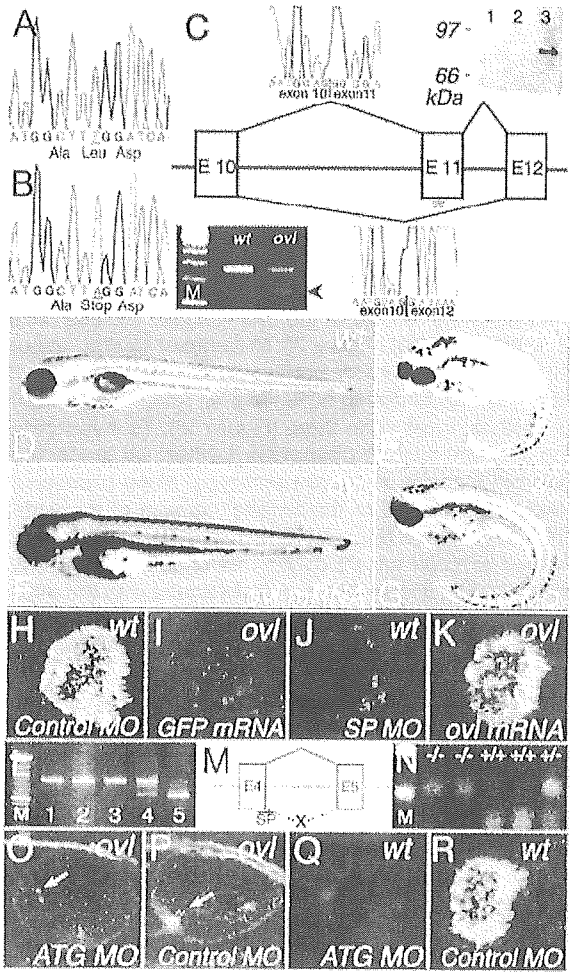

Figure 2. *ovl* Encodes a Zebrafish Homolog of the *ift88* Gene

(A and B) The genomic sequence of the *ovl*^{tz288b} mutation site in wt (A) and *ovl* (B). The T→A substitution introduces a premature stop codon in exon 11 of *ovl*.

(C) A schematic diagram of the splicing defect caused by the *ovl*^{tz288b} mutation: a premature stop codon in *ovl*^{tz288b} causes exon skipping. Lower left inset: RT-PCR analysis of mutant transcripts. The upper band in the *ovl* lane is the normal splice product while the lower one corresponds to the transcript missing exon 11 (arrowhead). DNA from each band was isolated and sequenced. The sequences of the normal length transcript (upper left inset) and the exon 11-deficient transcript (lower right inset) are provided. Upper right inset: Western blot of embryonic extracts from 2-cell stage wild-type embryos (lane 1), *ovl* mutant homozygotes at 3 dpf (lane 2), and wild-type larvae at 3 dpf (lane 3).

(D) A wild-type zebrafish larva at 72 hpf.

(E) An *ovl*^{tz288b} mutant homozygote at 72 hpf.

(F) *ift88* mRNA injections into *ovl*^{tz288b} mutant homozygotes rescue the wild-type phenotype.

(G) Anti-*ift88* morpholino (ATG) injections phenocopy the abnormal body axis curvature of the *ovl*^{tz288b} mutant homozygotes.

(H–K) Nasal pits of larvae at 72 hpf, stained with anti-acetylated α-tubulin antibody.

(H) Control morpholino does not affect olfactory cilia in wild-type zebrafish larvae.

(I) Control GFP mRNA injections do not affect the *ovl*^{tz288b} phenotype.

(J) Injections of anti-*ift88* morpholinos into wild-type embryos cause a loss of cilia.

(K) *ift88* RNA injections into the *ovl*^{tz288b} mutant homozygotes restore olfactory cilia.

(L) RT-PCR analysis shows that anti-*ovl* splice site (SP) morpholino blocks normal splicing of intron 4. Morpholino injection into wild-type embryos blocks splicing at 36 hpf (lane 1), 48 hpf (lane 2), and 72 hpf in embryos that display the *ovl*-like curled body axis (lane 3). Splicing is blocked partially in embryos that display a normal body axis at 72 hpf (lane 4). Control morpholino-treated embryos show normal splicing product at 48 hpf (lane 5).

(M) A schematic diagram of the intron 4 excision defect caused by SP morpholino.

(N) In rescue experiments, embryos were genotyped using the MTJM10RFLP polymorphism. *Bcl* I digestion product of DNA from *ovl*^{tz288b} homozygotes contains the longer DNA fragments only.

(O and P) Anti-*ovl* morpholino injections into *ovl*^{tz288b} homozygous animals produce the same phenotype (O) as a control morpholino (P) in the otic vesicle at 40 hpf. Embryos were stained with an anti-acetylated-α-tubulin antibody to visualize cilia (green) and rhodamine-conjugated phalloidin to visualize filamentous actin (red). In these experiments, the presence of olfactory cilia at 72 hpf was used to monitor the efficiency of morpholino injections.

(Q) ATG morpholino phenocopied the *ovl* olfactory cilia phenotype.

(R) A control morpholino did not affect olfactory cilia.

In (H)–(K) and (O)–(R), cilia are visualized by an anti-α-tubulin antibody staining. (D)–(G) show Nomarski optics images of larvae at 72 hpf, anterior is left, dorsal is up. In (O) and (P), cilia of tether cells are indicated by arrows. M, size marker lanes.

Table 1. Morpholino Phenocopy of the *ovl* Phenotype

MO Injected	Curved Body Axis	Kidney Cysts	Nasal Cilia Defect
ATG	101/113 (89%)	74/113 (65%)	9/12 (75%)
SP	37/88 (42%)	22/88 (25%)	9/13 (69%)
Control	3/112 (3%)	2/112 (2%)	0/13 (0%)

that rescued embryos are homozygous for the *ovl*^{tz288b} allele, we genotyped them using the MTJM10RFLP polymorphic marker (Figure 2N). *ift88* mRNA expression corrects the body axis defect and restores olfactory cilia at 3 dpf (Figures 2F and 2K, Table 2). In contrast, control injections of GFP mRNA do not affect the *ovl* mutant phenotype (Figure 2I, Table 2). Taken together, these experiments provide convincing evidence that a defect of the zebrafish *ift88* homolog is responsible for the *ovl*^{tz288b} mutant phenotype.

The Ovl polypeptide is enriched at the base of cilia in zebrafish larvae (Figures 3E and 3G). Consistent with the nature of the *ovl*^{tz288b} defect, this staining is not detectable in mutant animals (Figures 3F and 3H). In rare cases, we have observed single cilia that continue to display the Ovl staining in mutant animals (Figure 3H). To investigate whether this residual staining is contributed maternally, we attempted to detect the Ovl polypeptide by Western blotting of protein extract from 2-cell stage wild-type embryos. Ovl protein is not detectable using this approach, arguing against the presence of a significant maternal contribution (Figure 2C, upper right inset).

Cilia Defect in the *ovl* Mutant Animals

The outer segment is a specialized structure that connects to the rest of the photoreceptor cell body via a narrow constriction that forms around a cilium. How does the absence of functional *ift88* affect photoreceptor cilia? To address this question, we examined whether cilia and basal bodies are present in *ovl* mutant photoreceptors by immunostaining with anti-acetylated α-tubulin antibodies, which label cilia, and anti-γ-tubulin

Table 2. Rescue of the *ovl* Body Axis Defect by *ift88* mRNA

	Body Axis Curvature		
mRNA Injected	Severe (180°–270°)	Moderate (90°–180°)	Normal (0°–90°)
GFP	23 (18.85%)	6 (4.92%)	93 (76.23%)
ift88	2 (3.45%)	7 (12.07%)	49 (84.48%)

antibodies, which label centrosomes. In wild-type photoreceptors at 3 dpf, the acetylated α-tubulin staining and the γ-tubulin staining colocalize at the apical termini of photoreceptor cell inner segments (Figure 3C). The Ovl staining also localizes to the same region (Figure 3E). In contrast, in the *ovl* retina, cilia as well as the Ovl staining are not detectable (Figures 3D and 3F). The loss of cilia staining is already evident by 60 hpf (data not shown), indicating that the cilia defect precedes outer segment formation. Although their cilia are absent, *ovl*^{tz288b} mutant photoreceptors display normal basal body staining in apical regions of photoreceptor inner segments (Figure 3D, green signal). These experiments indicate that the loss of *ovl* affects the assembly of photoreceptor cilia but leaves the basal body intact. Apart from the absence of outer segment formation, the *ovl* photoreceptor cell morphology appears normal (Figure 3B, compare to the wild-type in 3A).

Cilia are also found on sensory cells of the vertebrate auditory and olfactory systems and are thought to be involved in otolith formation (Riley et al., 1997). Indeed, we found that in *ovl* mutants, otoliths display a higher frequency of defects. Approximately 70% (108/156) of wild-type embryos from the *ovl*/+ × *ovl*/+ cross have 2 otoliths at 1 dpf (Figure 3I). In contrast to that, about 40% (21/54) of *ovl*/*ovl* homozygous embryos have 2 otoliths. The remaining 60% have an abnormal number of otoliths, most often three (Figure 3J). To investigate the auditory system phenotype further, we inspected hair cell kinocilia in mutant embryos. Many prominent kinocilia are found in the anterior macula of the wild-type ear at 4 dpf (Figure 3K, n = 5), and the cristae of ear semicircular canals contain patches of particularly long kinocilia (Figure 3M, n = 5). In contrast to the wild-type ear, we do not detect any kinocilia staining in anterior maculae (Figure 3L, n = 7) and cristae (Figure 3N, n = 4) of *ovl* homozygotes at this stage.

In addition to photoreceptors and hair cells, cilia are also present in olfactory sensory neurons (Hansen and Zeiske, 1993). Consistent with the analysis of the visual

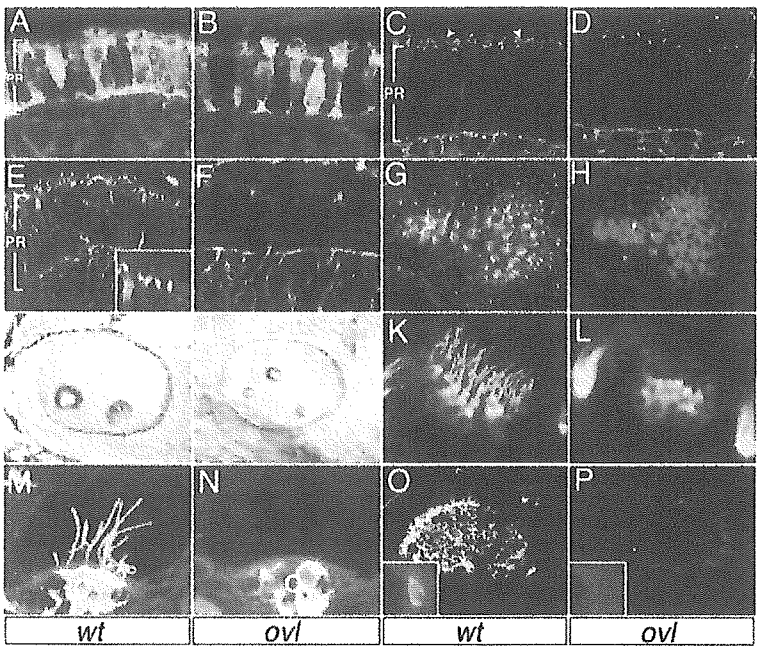

Figure 3. Cilia Defect in Mutant Sensory Neurons

(A and B) Transverse cryosections through wild-type (A) and *ovl* (B) retinae stained with the Zpr-1 antibody, which visualizes the cell membrane of red/green double cones.

(C) Photoreceptor connecting cilia (blue signal, arrowheads) are positioned just apical to basal bodies, here stained with an anti-γ-tubulin antibody (green).

(D) In *ovl* retinae at 3 dpf, basal bodies are positioned correctly but connecting cilia are not found.

(E) Ovl (red) colocalizes with connecting cilia (elongated green structures) in wild-type retinae at 3 dpf. Inset shows an enlargement.

(F) In *ovl* mutant retinae, both the Ovl polypeptide and connecting cilia are not detected.

(G and H) The apical surface of posterior maculae in ears of wild-type (G) and mutant (H) larvae at 76 hpf. Hair cells are visualized by phalloidin staining (red). In wild-type hair cells, the Ovl polypeptide is concentrated in bright foci. Ovl staining is largely absent in mutant animals.

(I) Two otoliths of approximately equal size are found in the otic vesicle in wild-type zebrafish at 1 dpf.

(J) Otic vesicles of *ovl* mutant animals frequently contain supernumerary otoliths in ectopic positions (arrow).

(K) Numerous cilia are observed in the anterior macula of the zebrafish ear at 4 dpf.

(L) No cilia are detected in the anterior macula of *ovl* mutants at 4 dpf.

(M) Anterior crista features long cilia at 4 dpf (green).

(N) In contrast to the wild-type, the *ovl* cristae do not contain cilia at this stage.

(O) Wild-type olfactory pits contain numerous cilia at 4 dpf.

(P) Cilia are largely missing in the *ovl* olfactory pits at 4 dpf.

In (C)–(F) and (K)–(P), cilia are visualized by staining with anti-acetylated α-tubulin antibody. Sections in (A), (B), (G), (H), (M), and (N) are counterstained with phalloidin (red). Insets in (O) and (P) show low-magnification views of olfactory pits. In (I) and (J), dorsal is up. In (A), (C), and (E), brackets indicate the approximate extent of photoreceptor cell layer. PR, photoreceptors; C, crista.

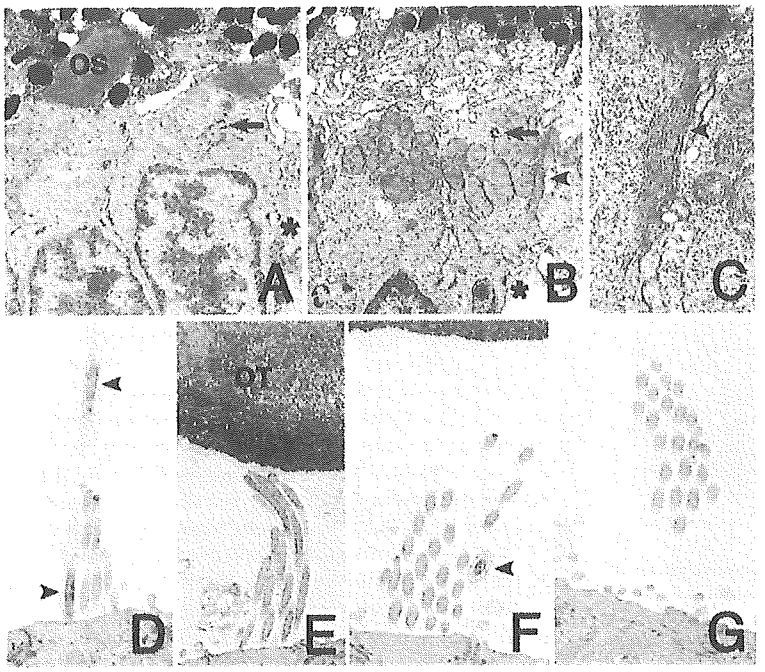

Figure 4. Ultrastructural Analysis of Sensory Cells

(A and B) Ultrathin sections through wild-type (A) and *ovl* (B) photoreceptor cells. Outer segments (OS) are well differentiated in wild-type animals at 88 hpf. In contrast to that, *ovl* photoreceptors do not form outer segments. Some photoreceptors form arrays of parallel membranes on their lateral surfaces (arrowhead).

(C) A magnification of membrane arrays at *ovl* photoreceptor lateral surface (arrowhead).

(D and E) Ultrathin sections through wild-type (D) and *ovl* (E) hair cells at 88 hpf. Both the kinocilium (arrowheads) and stereocilia are well differentiated in the wild-type (D). In contrast to that, *ovl* hair cells do not form kinocilia.

(F and G) Ultrathin sections across wild-type (F) and *ovl* (G) hair cell ciliary bundles. Numerous stereocilia and a kinocilium (arrowhead) are evident in the wild-type. In contrast to that, mutant ciliary bundles consist of stereocilia only.

In (A)–(C), retinal pigmented epithelium is up, asterisks indicate cell junctions, and arrows indicate basal bodies. In (D)–(G), otolith (OT) is up.

and auditory systems, we found that the mutant olfactory epithelium displays a dramatic loss of acetylated α-tubulin staining at 52 hpf compared to the wild-type (n = 4 for the wild-type, 4 for *ovl*, data not shown). This phenotype persists at 4 dpf (Figures 3O and 3P, n = 3 for the wild-type, 3 for *ovl*). We conclude that sensory cilia are absent in visual, auditory, and olfactory systems of *ovl* mutants.

Does the *ovl* mutation affect other aspects of sensory cell morphology? Electron microscopic analysis reveals that wild-type photoreceptors feature robust outer segments at 3 dpf (Figure 4A). In contrast to that, both at 72 and 88 hpf, *ovl* mutant photoreceptor cells do not differentiate outer segments (Figure 4B and data not shown). In some cases, we have observed parallel arrays of 10–20 membranes on the lateral surface of photoreceptor inner segments at 88 hpf (Figure 4C). These structures may represent outer segment membranes that assemble ectopically in the absence of IFT transport. Apart from these defects, *ovl* photoreceptor cells are healthy by at least two criteria: they form normal junctions of the outer limiting membrane, and their inner segments contain prominent clusters of mitochondria. Similar to photoreceptors, the auditory hair cell defect appears confined to cilia. While *ovl* kinocilia are absent at 88 hpf, hair cell stereocilia (despite their name, these are not true cilia) are indistinguishable from wild-type ones (Figures 4E and 4G, compare to the wild-type in Figures 4D and 4F).

ovl Function Is Not Required for the Initial Formation of Cilia

The lack of cilia in differentiated sensory structures could be due to the lack of cilia maintenance or to the absence of cilia formation. To test which is the case, we performed staining of sense organs with anti-acetylated α-tubulin antibodies at earlier stages of development. As the external *ovl* phenotype is not obvious prior to 48 hpf, mutant and wild-type embryos were distinguished by PCR genotyping of the MTJM10RFLP polymorphism. To our surprise, cilia form normally in the *ovl* ear at 40 dpf (Figure 5B, compare to the wild-type in 5A). Likewise, the loss of *ovl* function does not affect tether cells, which most likely represent the first hair cells, and are characterized by particularly long cilia (Figures 5A and 5B, insets; Riley et al., 1997). Similarly, in the retina of the *ovl* mutant homozygotes, cilia of neuroepithelial cells at 30 hpf are indistinguishable from the wild-type ones (Figures 5C and 5D). Finally, we examined olfactory cilia at an early stage of development. Cilia of the zebrafish olfactory epithelium first become visible at ~30 hpf (Hansen and Zeiske, 1993). Staining experiments reveal no difference between the *ovl* and wild-type olfactory cilia at 36 hpf (Figures 5E and 5F). Based on these observations, we conclude that *ovl* function is not necessary in sensory organs for cilia formation.

One explanation for the presence of cilia at early stages of development is that the *ovl*^{tz288b} mutant allele produces a partially functional polypeptide. If this unlikely scenario is correct, the injections of anti-*ovl* morpholinos into *ovl*^{tz288b} mutant homozygotes would enhance the mutant phenotype. This is not the case. The injections of anti-*ovl* morpholinos into *ovl*^{tz288b} mutants do not affect the cilia phenotype in the otic vesicle at 40 hpf, and the external appearance of mutant embryos remains the same as in control animals (Figures 2O and 2P and data not shown). As morpholino injections produce the mutant phenotype even in wild-type animals, the genotype of each embryo was confirmed by PCR using the MTJM10RFLP polymorphism. The injections of anti-*ovl* morpholinos produced the characteristic abnormal body curvature in 84% (37/44) of animals, whereas control morpholino injections resulted in 22% (10/45) of animals with this phenotype, a value expected

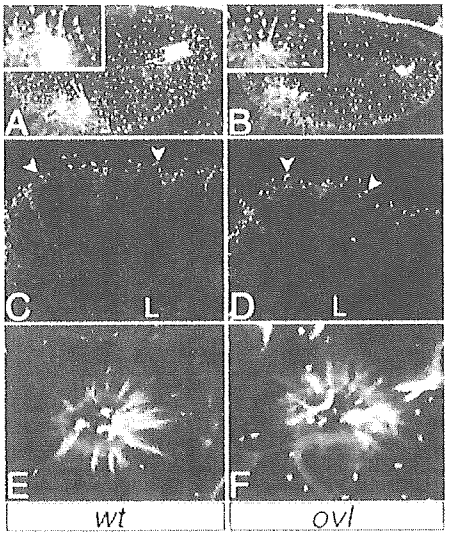

Figure 5. Normal Ciliogenesis in *ovl* Sensory Organs at Early Stages of Embryogenesis

(A) Cilia (green) in wild-type zebrafish otic vesicles at 40 hpf.

(B) Cilia in *ovl* otic vesicles are indistinguishable from these in the wild-type.

(C) Wild-type retinal neuroepithelium displays cilia on the apical surface at 30 hpf (arrowheads).

(D) Retinal cilia of *ovl* mutants (arrowheads) have the same appearance as the ones in the wild-type at 30 hpf.

(E) Olfactory pits of wild-type zebrafish embryo contain cilia (green) at 36 hpf.

(F) The olfactory cilia in *ovl* mutant animals appear identical to those in the wild-type.

(A), (B), (E), and (F) are counterstained with rhodamine-conjugated phalloidin (red). Insets in (A) and (B) show cilia of so-called tether cells. In (A) and (B) dorsal is up. L, lens.

based on the Mendelian segregation of the *ovl* defect. In addition, anti-*ovl* morpholino-treated wild-type progeny of the *ovl*/+ × *ovl*/+ crosses showed nasal cilia degeneration at 72 hpf (Figures 2Q and 2R), indicating that the morpholino treatment was effective. The above results, combined with the molecular nature of the *ovl*^{tz288b} defect, strongly suggest that *ovl*^{tz288b} is a null allele and indicate that sensory cell cilia are initially generated even in the complete absence of *ovl* function.

ovl Function Is Necessary for the Survival of Sensory Cells

The initial characterization of the *ovl* phenotype revealed a gradual degeneration of the photoreceptor cell layer starting at 3 dpf (Doerre and Malicki, 2002). As we demonstrate in this paper, this phenotype is preceded by the loss of cilia. Is the cilia defect also followed by a degeneration of other sensory cells? To address this question in the auditory system, we evaluated the occurrence of cell death in ears of *ovl* mutants at 72 hpf using the TUNEL detection method. These experiments revealed a substantial increase of cell death in ears of mutant animals (Figures 6C–6E). To evaluate the extent of hair cell death, we prepared plastic sections through both anterior and posterior sensory maculae at 3 and 5 dpf. The sensory maculae of the zebrafish inner ear consist of two cell types: sensory hair cells and the supporting cells (Haddon and Lewis, 1996). Hair cells can be identified on histological sections by a larger size and the apical location of their nuclei (Figure 6F, inset). By contrast, the supporting cells appear smaller and have their nuclei positioned basally. We counted hair cell numbers on sections through posterior and anterior maculae. At 3 dpf, the number of hair cell nuclei in posterior maculae of *ovl* mutant animals is fairly normal. The average of 4.5 and 3.8 hair cells per section are found in wild-type and *ovl* posterior maculae, respectively (Figures 6F, 6G, and graph in 6J). Similarly, the number of hair cells in the anterior macula also appears largely unaffected (Figure 6J). By 5 dpf, however, mutant hair cell count in the posterior macula decreases dramatically to the average of 0.3 cells per section, while the number of hair cells in the wild-type increases to 5.4 cells (Figures 6H, 6I, and graph in 6J). A decrease of a similar magnitude is also obvious in the *ovl* anterior macula (Figure 6J). These observations indicate that *ovl* function is necessary for hair cell survival. The loss of hair cells is delayed relative to the loss of kinocilia. Already by 2 dpf, the number of kinocilia is reduced by more than 50% in mutant maculae (Figure 6J). This deficit becomes even more severe at later stages. While the average of 35 kinocilia are found in the wild-type by 3 dpf (n = 5), *ovl* mutant embryos display, on average, only 2 kinocilia per macula (n = 7; Figure 6J, face view). At 4 dpf, no kinocilia are observed in the maculae of *ovl* mutants (n = 6), whereas the average of 52 kinocilia are found in the wild-type (n = 5; Figure 6J, face view). In contrast to kinocilia, the loss of stereocilia largely correlates with hair cell death. At 3 dpf, the *ovl* stereocilia remain largely intact as evidenced by phalloidin staining (Figures 6A and 6B) and electron microscopy (Figures 4D–4G). As kinocilia of auditory maculae are nearly entirely missing by 3 dpf, hair cell degeneration in *ovl* may be a secondary consequence of cilia defect.

Does the loss of *ovl* function also affect olfactory neurons? Olfactory sensory neurons extend olfactory knobs into the nasal pit and can be labeled by DiI (Dynes and Ngai, 1998; Hansen and Zeiske, 1993). In wild-type fish, strong DiI staining is observed in olfactory pits at 4 dpf (Figure 6K), while little or no staining is seen in sibling *ovl* mutant homozygotes at the same stage (Figure 6L). This observation indicates that olfactory neurons are abnormal in the *ovl* animals. The absence of DiI staining in the *ovl* mutants may, however, be caused by the lack of cilia or by an abnormality of olfactory knobs. To determine whether olfactory sensory neurons persist in *ovl* mutants, we performed in situ hybridization to detect *olfactory marker protein* (*omp*) transcript, which is specifically expressed in mammalian and zebrafish olfactory sensory neurons (Yoshida et al., 2002). At 3 dpf, *omp* is expressed in the nasal pits of both wild-type (n = 11) and *ovl* (n = 10) animals, indicating that olfactory sensory cells are still present in the mutant at this stage (Figures 6M and 6N). By contrast, at 5 dpf only a small fraction of *ovl* embryos display normal *omp* expression (2/17), while the majority (11/17) do not express *omp* at all (Figure 6P). *omp* is expressed in all wild-type control embryos at this stage (n = 16, Figure 6O). A control

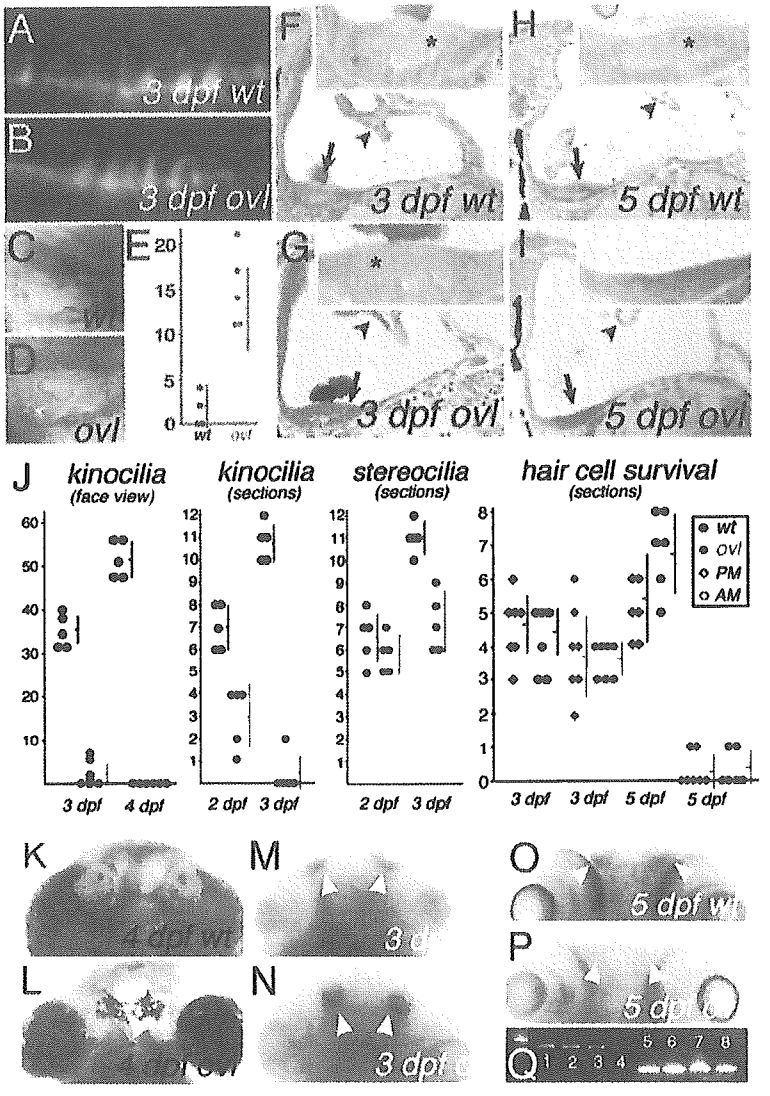

Figure 6. Loss of Sensory Cells in *ovl*

(A and B) Optical sections through anterior maculae in whole mounts of wild-type (A) and *ovl* (B) embryos at 3 dpf. Kinocilia are visualized using anti-acetylated α-tubulin antibody (red) and stereocilia by phalloidin staining (green). Both kinocilia and stereocilia are well differentiated in wild-type animals (A). By contrast, *ovl* kinocilia are missing.

(C and D) TUNEL detection of cell death in ears of wild-type (C) and *ovl* (D) larvae. The number of dying cells (green dots) is elevated in the mutant already by 3 dpf. Arrowhead indicates a crista.

(E) Quantitation of the result shown in (C) and (D). Cell death is clearly elevated in mutant animals ($p \leq 0.000329$).

(F) A row of hair cells is distinguishable on histological sections through the posterior macula (arrow) at 3 dpf. Inset shows an enlargement of sensory epithelium. Hair cells (asterisk) localize apically, display an ellipsoid shape, and stain somewhat lighter than surrounding cells.

(G) At 3 dpf, the posterior macula of *ovl* mutant animals is similar to the one in the wild-type.

(H) Hair cells are easily distinguishable on histological sections through the posterior macula (arrow) at 5 dpf.

(I) The number of hair cells is drastically reduced in the posterior macula of *ovl* mutants at 5 dpf.

(J) The loss of cilia precedes hair cell degeneration. Kinocilia counts were performed following whole-mount staining of embryos with anti-acetylated α-tubulin antibody using either transverse optical sections or apical surface views (face view) of anterior maculae. Stereociliary bundles were counted using transverse optical sections through the anterior macula. Hair cell counts were performed on plastic sections through anterior and posterior maculae such as the ones shown in (F)–(I). In all graphs, each dot represents a separate individual.

(K) Wild-type olfactory pits display strong DiI staining at 4 dpf.

(L) In contrast to the wild-type, DiI staining is not observed in *ovl* nasal pits (arrowhead).

(M) In situ hybridization using the *omp* probe reveals the presence of olfactory sensory neurons in wild-type olfactory pits at 3 dpf.

(N) The *omp* staining in *ovl* mutants is not distinguishable from the one in wild-type embryos.

(O) The *omp* transcript continues to be expressed in wild-type nasal pits at 5 dpf.

(P) Compared to the wild-type, the *omp* expression is much reduced in *ovl* mutants at 5 dpf.

(Q) RT-PCR analysis of *omp* expression: the *omp* transcript (lanes 1–4); β-*actin* transcript (lanes 5–8). Lanes 1, 2, 5, and 6 show RNA at 3 dpf. Lanes 3, 4, 7, and 8 show RNA at 5 dpf. Wild-type RNA is shown in odd-numbered lanes. *ovl* RNA is analyzed in even-numbered lanes. The *omp* transcript is absent from *ovl* embryos at 5 dpf.

In (C) and (D) dorsal is up. In (F)–(I), arrows indicate the posterior macula, arrowheads point to the ridge that separates the lateral and posterior semicircular canals, inset asterisks indicate hair cell nuclei, midline is down, dorsal is right. In (K)–(P) anterior is up. In (L)–(P) arrowheads indicate olfactory pits. PM, posterior macula; AM, anterior macula.

kidney-expressed transcript is detected at the same level in *ovl* and wild-type animals (data not shown). Semiquantitative RT-PCR analysis also shows that *omp* expression is decreased below the detection level in *ovl* at 5 dpf (Figure 6Q). These results strongly suggest that olfactory sensory neurons are absent in *ovl* mutant animals by 5 dpf. Based on these observations, we conclude that sensory cells in three different sensory organs, the eye, the ear, and olfactory pits, degenerate following the loss of cilia.

Other Components of the IFT Particle also Function in Sensory Cells

The IFT particle is composed of at least 17 polypeptides that assemble into two complexes: A and B (reviewed in Rosenbaum and Witman, 2002). *ovl/ift88* belongs to the IFT complex B, which consists of at least 12 proteins. To examine the function of other IFT complex B and A components, we cloned four zebrafish genes: *ift20, ift52, ift57*, and partially *ift140* using RT-PCR. To investigate the role of *ift57* in sensory cell cilia development, we

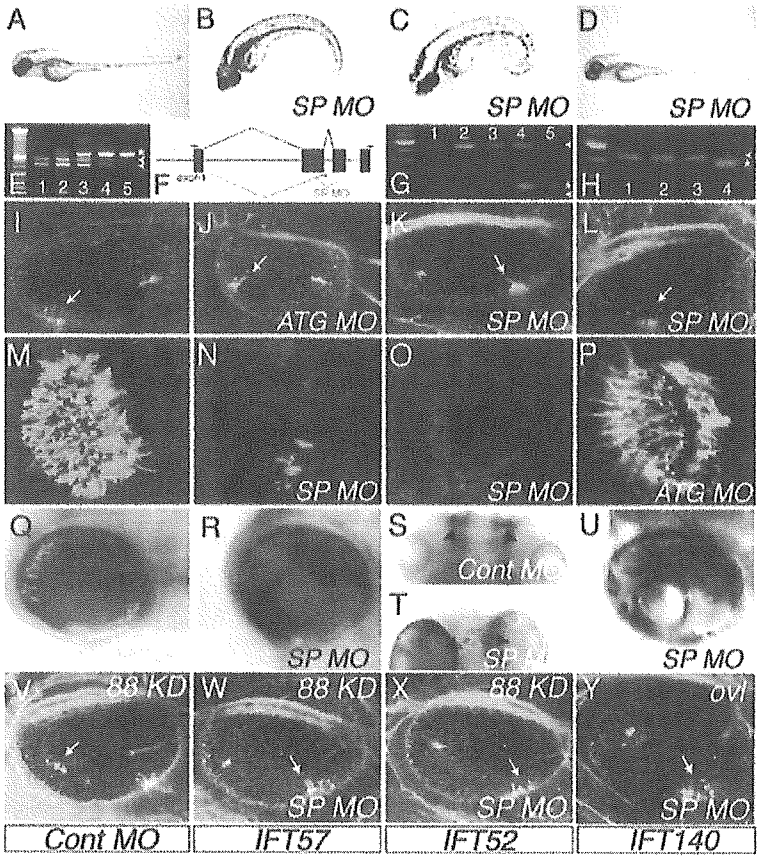

Figure 7. Knockdown Phenotypes of IFT Genes

The external phenotype of morpholino knockdown animals.

(A) Control morpholino injections do not affect body axis of wild-type embryos.

(B and C) *ift57* and *ift52* splice site morpholinos induce abnormal body axis curvature.

(D) *ift140* morpholinos do not produce consistent body axis defects.

(E) RT-PCR analysis of *ift57*SP knockdown efficiency at 36 hpf (lane 1), 48 hpf (lane 2), 72 hpf (lane 3, embryos that display abnormal body axis curvature), 72 hpf (lane 4, embryos that display normal body axis). Control morpholino does not affect transcript size at 48 hpf (lane 5).

(F) A schematic diagram of *ift57*SP morpholino-induced splicing defect. Knockdown results in two abnormal splicing products (blue lines). Morpholino (MO) target is indicated in red.

(G) RT-PCR analysis of *ift52*SP knockdown efficiency at 48 hpf (lane 1), 60 hpf (lane 2), 72 hpf (lane 3, embryos that display abnormally curved body axis), 72 hpf (lane 4, embryos that display normal body axis). Control morpholino does not affect transcript size at 48 hpf (lane 5).

(H) RT-PCR analysis of *ift140*SP knockdown efficiency at 48 hpf (lane 1), 60 hpf (lane 2), 72 hpf (lane 3). Control morpholino does not affect transcript size at 48 hpf (lane 4).

(I–L) Neither control morpholino (I) nor IFT-targeted mopholino knockdowns produce cilia defects in the otic vesicle at 40 hpf. Note that in all cases tether cells are not obviously affected (arrows).

(M) A control morpholino knockdown does not affect olfactory cilia.

(N–P) IFT-targeted morpholinos produce a loss of cilia. The *ift140* knockdown phenotype is much weaker compared to *ift57* and *ift52*.

(Q) A control morpholino knockdown does not affect GFP expression in the eye.

(R) *ift57*SP morpholino results in a loss of GFP expression at 4 dpf.

(S) Control morpholino does not affect *omp* expression in nasal pits at 5 dpf.

(T) *ift52*SP morpholino knockdown results in a sharp decrease of *omp* expression.

(U) GFP expression remains largely unaffected in *ift140* knockdown animals.

(V) Gene function knockdown using an anti-*ift88/ovl* morpholino combined with a control morpholino produces a phenotype of the same severity as the *ift88* knockdown alone at 42 hpf.

(W) Ear phenotype of *ift57/ift88* double knockdown animals at 42 hpf.

(X) Ear phenotype of *ift52/ift88* double knockdown animals at 42 hpf.

(Y) Ear phenotype of *ift140* knockdown performed in *ovl* mutant homozygotes at 42 hpf.

In (I)–(L) and (V)–(Y), embryos are counterstained with rhodamine-conjugated phalloidin (red). In (I)–(P) and (V)–(Y), cilia are visualized with anti-acetylated α-tubulin antibody (green). In (A)–(D), (Q), (R), and (U), anterior is left, dorsal is up. In (S) and (T), anterior is up, arrowheads indicate nasal pits. In (E), (G), and (H), asterisks indicate wild-type transcripts, arrows indicate morpholino-induced splicing products. In (V)–(X), *88KD* indicates *ift88* knockdown.

designed ATG and splice site (SP) morpholinos targeted to its open reading frame. Sequence analysis of the *ift57* RT-PCR amplification product reveals that the SP morpholino interferes with the splicing of exon 2, producing two shorter transcripts (Figures 7E and 7F). One of these contains a deletion of the entire exon 2, the second a deletion of the 3′ region of exon 2 (Figure 7F). Both morpholino-induced transcripts contain frameshifts in the *ift57* open reading frame, resulting in a truncation of approximately 75% of the *ift57* polypeptide. Anti-*ift57*SP morpholino completely suppresses normal splicing until at least 36 hpf and results in a partial splicing suppression until 48 hpf (Figure 7E).

At 40 hpf, the development of cilia in the otic vesicle of *ift57* knockdown animals is indistinguishable from that in control morpholino-injected fish (Figure 7J, compare to 7I, Table 3). Both ATG and SP anti-*ift57* morpholinos produce *ovl*-like curved body axis (Figure 7B, Table 3) and a loss of olfactory cilia at 72 hpf (Figure 7N, compare to 7M, Table 3). These results demonstrate that *ift57* is not necessary for the generation of cilia but is required for their maintenance. To investigate the role of *ift57* in sensory neuron survival, we injected *ift57*SP morpholino into a zebrafish strain that carries a GFP transgene driven by the rhodopsin promoter (Fadool, 2003). This transgene expresses GFP in rod photoreceptor cells. In control morpholino-injected fish, GFP is expressed in a punctate pattern characteristic of devel-

Table 3. Summary of the IFT Knockdown Phenotypes

	Presence of Ear Cilia (36–40 hpf)	Curved Body Axis[a] (72 hpf)	Loss of Nasal Cilia (72 hpf)	Rodopsin-GFP Expression (4 dpf)[b]
*ift57*ATG	3/3 (100%)	21/57 (37%)	4/4 (100%)[c]	ND
*ift57*SP	6/6 (100%)	21/34 (62%)	8/8 (100%)	0/6 (0%)
*ift52*ATG	3/3 (100%)	46/49 (94%)	5/5 (100%)	ND
*ift52*SP	4/4 (100%)	90/111 (81%)	5/5 (100%)	0/6 (0%)
*ift140*ATG	ND	5/146 (3%)	2/6 (33%)[d]	ND
*ift140*SP	4/4 (100%)	7/124 (6%)	1/6 (16%)[d]	9/9 (100%)[e]
Control	5/5 (100%)	4/139 (3%)	0/6 (0%)	9/9 (100%)

Format of entries: number of individuals that display a given phenotype/total number of individuals inspected (percentage value).
[a] Body axis curved more than 90°.
[b] Result obtained using rhodopsin-GFP transgenic fish. In some individuals residual GFP expression persists in the ventral retina.
[c] This morpholino did not produce a complete loss of cilia.
[d] Only anterior part of nasal pit affected.
[e] Expression level reduced.
ND: not determined

oping rod photoreceptors at 4 dpf (Figure 7Q, Table 3). By contrast, in *ift57*SP morpholino-treated fish, almost no GFP expression is observed, except for a small patch of cells in the ventral region of the retina (Figure 7R, Table 3; Fadool, 2003). These observations suggest that rod photoreceptors degenerate in *ift57* gene product-deficient fish.

Similar results were obtained in the *ift52* knockdown experiments. The *ift52*SP morpholino effectively blocks normal splicing at least until 48 hpf (Figure 7G). It produces two aberrant splicing products: a longer transcript that retains an intron, and a shorter transcript that contains a small deletion resulting from an activation of an ectopic donor splice site. Both splicing defects are predicted to produce truncated polypeptides that lack 80% of the wild-type amino acid sequence. Similar to *ovl/ift88* and *ift57* phenotypes, otic vesicle cilia are not affected by the *ift52* knockdown at 40 hpf (Figure 7K, Table 3). Both morpholinos, however, produce an abnormally curved body axis and nasal cilia degeneration at 72 hpf (Figures 7C and 7O, Table 3). The injection of SP morpholino into rhodopsin-GFP transgenic zebrafish produces a dramatic reduction of GFP expression (Table 3 and data not shown). Olfactory sensory neurons are also affected. At 5 dpf, only a small fraction of the *ift52* SP morpholino-injected embryos display normal *omp* expression (2/11), while the majority (9/11) do not express *omp* at all (Figure 7T). *omp* is expressed at the normal level in all control morpholino-injected embryos (n = 17, Figure 7S). Thus, also *ift52* is not necessary for the initial generation of cilia, but is required for their maintenance and the maintenance of sensory cells themselves.

In contrast to the complex B components, the knockdown of *ift140*, a complex A polypeptide, produces a much weaker phenotype. In 16% of SP morpholino-injected fish, the tail is curved slightly upwards (not shown), and only 6% of them show *ovl*-like ventral curling of the body axis that exceeds 90° (Table 3). This percentage is roughly the same as in control animals. The majority of the *ift140* morphants display a normal shape of body axis (Figure 7D), and their otic vesicle cilia appear normal (Figure 7L). In ATG morpholino-injected animals, upward curving of the tail is not observed and only 3% of them show ventrally curled body axis (Table 3). The olfactory cilia defect is also weaker. In both ATG morpholino- and in SP morpholino-treated embryos, the density of cilia is reduced mainly in the anterior portion of the nasal pit at 72 hpf (Figure 7P, Table 3). These defects are relatively infrequent and cilia are mostly normal in the posterior regions of the olfactory epithelium. Cilia are also not very well developed in the anterior part of the nasal pit at 60 hpf (data not shown, n = 5 for ATG MO, n = 5 for SP MO), but their appearance is normal at 36 hpf in *ift140*SP (n = 4) and *ift140*ATG (n = 4) morpholino-injected fish (data not shown). We also tested the role of *ift140* in neuronal survival using rhodopsin-GFP transgenic fish. In contrast to *ift52* or *ift57* knockdowns, GFP expression was only weakly affected at 4 dpf (Figure 7U, Table 3).

The SP morpholino *ift140* knockdown produces a somewhat longer transcript and a complete or near-complete loss of the wild-type splicing product at least until 72 hpf (Figure 7H). Cloning and sequencing of the morpholino-induced transcript reveals an insertion of 33 bp that contains two in-frame stop codons, which are predicted to result in a truncation of the *ift140* gene product within the first 90 amino acids. Thus, the *ift140* knockdown is likely to result in a complete loss of function. The *ift140* knockdown experiments indicate that this gene is not absolutely required for cilia maintenance at least during early larval development. This contrasts with our findings for the IFT complex B proteins, Ift52, Ift57, and Ift88, which appear to play more fundamental roles.

Although the IFT complex B components are not obviously related to each other on the protein sequence level, it remains possible that they function redundantly in the initial formation of cilia. To investigate this possibility, we performed double knockdowns of *ift57* and *ovl*, as well as *ift52* and *ovl*. Double knockdown experiments produce phenotypes that are indistinguishable from knockdowns of single genes (Figures 7W and 7X). These results argue that a functional redundancy of *ovl* and other IFT complex B components is unlikely to account for the initial formation of cilia in *ovl* mutants. Another scenario that should be considered is that a deficiency of both an IFT complex A protein (Ift140) and a complex B component (Ovl) produces a synergistic effect and a much stronger phenotype than single gene defects. To

test this possibility, we injected *ift140*SP morpholino into *ovl*^{tz288b} mutant homozygotes. This treatment does not affect the appearance of otic vesicle cilia at 36 or 42 hpf (Figure 7Y; n = 12), indicating that the initial cilia formation proceeds even in the absence of both complex A and complex B components.

Ectopic Accumulation of Rod Opsin Contributes to Photoreceptor Loss

Opsin polypeptides are the most abundant protein components of the photoreceptor outer segment. Mouse or salamander rod outer segments are estimated to contain 10^8 and 3×10^9 of opsin molecules, respectively (Pugh and Lamb, 2000). The lack of outer segment formation in *ovl* animals is thus likely to result in the accumulation of rod opsin in the photoreceptor cell body. This is, indeed, the case (Figure 8K, compare to 8J). The ectopic accumulation of rod opsin outside the outer segment may thus contribute to photoreceptor lethality. To test whether this is the case, we decided to reduce rod opsin expression levels using morpholino oligonucleotides and to investigate how this treatment affects photoreceptor survival. Western blotting of embryonic extracts confirmed that rod opsin levels are lower in rod opsin morpholino-treated embryos at 3 dpf, compared to control morpholino-treated animals (Figure 8C, inset). Indeed, lowering opsin expression results in an improved rod photoreceptor survival (Figure 8A, compare to 8B). On average, over 50% more rods survive in rod opsin morpholino-treated *ovl* animals, compared to mutants treated with a control morpholino (Figure 8C, $p \leq 0.000214$). This effect appears to be specific to rods, as the survival of red/green double cones is not significantly affected (Figure 8C, $p \leq 0.186$). These results indicate that the ectopic accumulation of opsin contributes to photoreceptor lethality in *ovl* mutants.

Ectopic accumulation of rod opsin polypeptide may be sufficient to cause enhanced photoreceptor lethality. Alternatively, lethality may be caused by the interference of light-activated rod opsin with intracellular signaling pathways in the inner segment or other parts of the photoreceptor soma. In the latter scenario, photoreceptor lethality in *ovl* mutant animals would be enhanced by light exposure. This is, in fact, the case. *ovl* mutants reared in constant darkness display slower photoreceptor loss, compared to individuals reared on a light/dark cycle or in constant light of 750 lux (Figures 8D–8F). *ovl* larvae exposed to constant light display a pronounced thinning of the outer nuclear layer at 108 hpf (Figure 8F), while larvae reared on a light/dark cycle exhibit a patchy pattern of cell loss in the ONL (Figure 8E). By contrast, animals kept in complete darkness display a nearly normal photoreceptor cell layer (Figure 8D). Constant exposure of *ovl* larvae to light enhances lethality of both red/green cones and rods by approximately 50%, compared to mutants reared in constant darkness (Figures 8G and 8H, $p \leq 4.73E\text{-}5$ for rods and 0.000512 for red/green cones). At 84 hpf, larvae that were exposed to constant light for 36 hr only also show significant loss of both rod and cone photoreceptors (Figures 8G and 8H, $p \leq 2.37E\text{-}5$ for rods and 0.00996 for r/g cones). Light intensity that was used in these experiments is not sufficient to cause photoreceptor loss in wild-type animals (Fig-

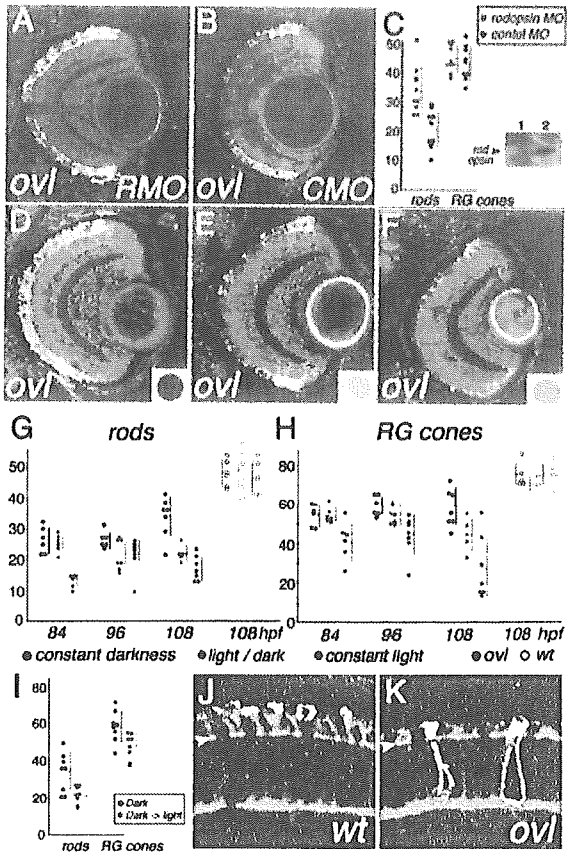

Figure 8. Light Dependency of Photoreceptor Loss in *ovl* Mutant Animals

(A and B) Transverse sections through retinae of an anti-rod opsin morpholino (A) and a control morpholino (B)-treated *ovl* mutant larvae at 108 hpf. Rod photoreceptors (green) and double cones (blue) are visualized by antibody staining. A downregulation of rod opsin expression enhances the survival of rod photoreceptor cells but has little effect on red/green double cones.

(C) Photoreceptor survival in anti-rod opsin (red dots) and control (black dots) morpholino-treated *ovl* mutants.

(D–F) Transverse sections through retinae of *ovl* mutant larvae at 108 hpf. Animals were reared in constant darkness (D), on light/dark cycle (E), or in constant light (F). Photoreceptor loss is much more severe after light exposure (E and F), compared to individuals reared in darkness (D).

(G and H) Rod photoreceptor (G) and red/green cone (H) survival in individuals reared in constant darkness (black dots), light/dark cycle (blue dots), and constant light (red dots). Light causes a severe increase of photoreceptor loss. Wild-type control animals have been analyzed at 108 hpf only (open circles).

(I) A quantitation of photoreceptor loss in retinae exposed to light from 96 to 108 hpf.

(J and K) Transverse cryosections through wild-type (J) and mutant (K) retinae at 72 hpf. Filamentous actin is visualized with phalloidin (red), rod opsin with antibodies (green). In *ovl* animals, rod opsin is distributed through the photoreceptor cell membrane. Arrowheads indicate OLM.

In (A), (B), and (D)–(F), tissue is counterstained with propidium iodide. In (C) and (G)–(I), each dot represents photoreceptor count from a single section; means and standard deviations are indicated by horizontal and vertical bars, respectively. RG cones, red/green cones; RMO, anti-rod opsin morpholino; CMO, control morpholino. A minimum of five individuals was used in each experiment.

ures 8G and 8H, open circles, $p \leq 0.180$ for rods and 0.461 for r/g cones). Even a short 12 hr exposure of *ovl* photoreceptors to light, from 96 hpf to 108 hpf, is sufficient to increase photoreceptor loss by 20%–30% (Figure 8I, $p \leq 0.00466$ for rods and 0.00712 for r/g cones). The same light treatment regimen does not affect photoreceptor survival in the wild-type ($p \leq 0.459$ for rods and 0.379 for r/g cones, data not shown). Although we cannot formally exclude the possibility that light-induced photoreceptor loss in *ovl* is due to the activation of other proteins, opsins are by far the most likely candidates for factors that mediate light damage. Accordingly, we postulate that the activation of ectopic opsin molecules in photoreceptor cells is a factor that strongly contributes to the lethality of this cell class in mutant retinae.

Discussion

Here we present several lines of evidence that the zebrafish *ovl* locus encodes a homolog of the *Chlamydomonas IFT88* gene: mapping studies, the characterization of the ovl^{tz288b} molecular defect in the *ift88* open reading frame, knockdown phenotype, and rescue experiments all support this conclusion. The *ovl* mutation provides a valuable opportunity to study the IFT particle function in the vertebrate central nervous system. Such studies are complicated in the mouse because the mouse *IFT88* null allele, $Tg737^{\Delta 2\text{-}3\beta Gal}$, causes embryonic lethality during midgestation, making it difficult to study neuronal differentiation and survival in mutant animals (Murcia et al., 2000). The $Tg737^{orpk}$ allele, on the other hand, is hypomorphic and gives a much weaker phenotype than that of ovl^{tz288b}: while $Tg737^{orpk}$ mice differentiate fairly robust outer segments, ovl^{tz288b} photoreceptors do not produce outer segments at all (Doerre and Malicki, 2002; Pazour et al., 2002). Thus, the role of *ift88* in photoreceptor development appears much more profound than previously assumed.

Previous experiments demonstrated that *IFT88* mutations cause a loss of cilia at very early stages of vertebrate embryogenesis. In the $Tg737^{\Delta 2\text{-}3\beta Gal}$ mice, ciliogenesis in sensory neurons could not be investigated, but the node cells lack cilia during embryonic day 7 (Murcia et al., 2000). Accordingly, we expected complete lack of cilia in the *ovl* mutant animals. Contrary to initial expectations, our studies indicate that cilia are generated at early developmental stages in the three sensory systems that we investigated. Knockdown analysis of other IFT complex B proteins also showed that cilia are generated normally in the otic vesicle even in the absence of the *ift52* or *ift57* functions. To monitor knockdown efficacy, we showed that normal splicing is completely or nearly completely blocked during the first 36 hr of development. These findings demonstrate that the zebrafish IFT complex B components are not required for the initial generation of cilia.

Our results show that the phenotypes of three IFT complex B components are very similar to each other, although the *ift52* knockdown defects appear somewhat stronger. In contrast to that, the knockdown of a complex A component, *ift140*, produces a markedly weaker phenotype. The most obvious difference is the lack of abnormal body axis curvature that characterizes the *ovl*, *ift52*, and *ift57* mutant phenotypes. Similarly, at later stages of development, the olfactory cilia defect is also less pronounced. These observations are consistent with genetic analysis in *C. elegans* that places complex A and B genes in different phenotypic categories: in contrast to the complex B-defective animals, mutants of the complex A components display cilia of nearly normal length (Perkins et al., 1986).

In nonvertebrate models, including *C. elegans* and *Drosophila*, the lack of *IFT88* function causes a loss of cilia in neurosensory cells (Han et al., 2003; Perkins et al., 1986). Death of sensory neurons has not been reported, however. In contrast to that, the *ovl* loss of function shows neuronal cell degeneration that follows cilia loss. This finding is interesting because a degeneration of photoreceptors or hair cells is frequently observed in inherited human disorders of the visual and auditory systems. IFT genes may thus be involved in human disease. The human *IFT52* gene maps to *20q13* and *IFT57* to *3q13*. Among the diseases that map to these regions, Bardet-Biedl Syndrome 3 (*BBS3*) is of particular interest since it is characterized by a retinal dystrophy and renal malformations (Green et al., 1989). Based on its map position on chromosome 3 between D3S1595 and D3S1302 (Ghadami et al., 2000), *IFT57* is a strong candidate for the *BBS3* gene.

The cause of sensory cell death in mutants of intraflagellar transport is not entirely clear. Photoreceptor cell loss in *ovl* mosaic retinae is cell autonomous, indicating that it is produced by a defect within photoreceptors (Doerre and Malicki, 2002). As the excess of opsin expression leads to photoreceptor degeneration (Tan et al., 2001), the accumulation of opsin in the photoreceptor cell body may contribute to photoreceptor lethality. Our experiments show that this is the case in *ovl* mutants. Moreover, photoreceptor loss in *ovl* animals appears to be enhanced by light-induced opsin activation. This result is consistent with previous cell culture studies, which led to the conclusion that ectopic opsin activation induces photoreceptor cell death by activating adenylyl cyclase (Alfinito and Townes-Anderson, 2002). Although quantities of signal transduction components in other sensory cells are lower than in photoreceptors, even small amounts of ectopic signal tranducers may contribute to sensory neuron lethality. Alternatively, sensory neurons could be eliminated because the lack of intraflagellar transport may render them nonfunctional. The absence of intraflagellar transport may affect visual and olfactory signal transduction cascades, both of which function in cilia or their derivatives (Makino et al., 2003; Zufall and Leinders-Zufall, 2000). The death of hair cells is the most difficult to explain, as the role of kinocilia is still poorly defined. Kinocilia are, in fact, absent in the cochlea of adult mammals (Sobkowicz et al., 1995).

Previous mutagenesis screens in zebrafish identified at least two other loci that display *ovl*-related phenotypes: *elipsa* and *fleer* (Doerre and Malicki, 2002; Malicki et al., 1996). Based on the results of morpholino knockdown experiments, IFT particle components may be encoded by these loci. It is also possible that *elipsa* and *fleer* encode other ciliary proteins, which have not been identified so far. Genetic analysis of zebrafish mutants is likely to further contribute to the understanding of

intraflagellar transport and its role in sensory neuron development and survival.

Experimental Procedures

Fish Strains

The maintenance and breeding of zebrafish strains and staging of embryonic development were performed as described previously (Kimmel et al., 1995; Malicki et al., 2002). The phenotype of whole embryos was observed using a Zeiss Axioscope microscope or Leica MZ12 dissecting scope. Images were recorded using digital or conventional cameras and processed with Adobe Photoshop software (Adobe, Inc.). The *ovl*^{tz288b} allele, originally recovered in a large-scale mutagenesis screen (Brand et al., 1996), was initially characterized in a previous study (Doerre and Malicki, 2002).

Mapping and Linkage Analysis

A map cross was set up between heterozygous carriers of the *ovl*^{tz288b} allele (AB genetic background) and wild-type WIK strain homozygotes. Half-tetrad analysis was used to determine the *ovl* linkage group (Streisinger et al., 1986). To determine the *ovl* map position further, we used a panel of 2495 F2 diploid embryos obtained via incrossing of F1 animals. To determine the segregation pattern of genomic polymorphisms, F2 embryos were digested in a lysis buffer (10 mM Tris-HCl [pH 8.3], 50 mM KCl, 0.3% Tween-20, 0.3% IGEPAL CA-630, 1 mg/ml Proteinase K), and the lysate was diluted 50× with water and used in PCR genotyping of simple sequence-length polymorphisms. PCR was carried out in a 20 μl reaction mixture containing 50 ng of genomic DNA, 10 pmol of each primer, 2.0 mM $MgCl_2$, 1× reaction buffer (Takara), 150 μM of each dNTP, and 1.0 U of EX Taq polymerase (Takara). Samples were amplified for 32 cycles, 30 s at 94°C, 30 s at 60°C, and 30 s at 72°C. PCR products were electrophoresed on 6% denaturing polyacrylamide gels for 2 hr. To genotype the intragenic Bcl I restriction fragment-length polymorphism MTJM10RFLP, we used primers ATGGTGCAGGATT GCCTATT and CTTTACATTGGGAGTCGGGT.

Cloning of IFT Proteins and Mutation Search

To identify the full-length zebrafish coding sequences of *ovl* and other *IFT* genes, human, mouse, *C. elegans*, and *Chlamydomonas* IFT protein sequences were obtained from the NCBI public database and analyzed using a homology search program, BLASTP, against the whole-genome zebrafish shotgun sequence database (Ensemble Database, Sanger Center, UK) and the BAC sequencing project database (Sanger Center). Based on partial sequences obtained in this manner, RT-PCR was performed to obtain the full-length gene products. Total RNA was extracted from 3 dpf wild-type and *ovl* embryos using Trizol regent (Invitrogen) and served for cDNA synthesis using Superscript II transcriptase (Invitrogen). Reverse transcription was performed in a 10 μl reaction volume, containing ~1 μg total RNA, 10 pmol oligo-dT_{25}, 5 mM of each dNTP, 20 μM DTT, and 50 units of Superscript II (Invitrogen) at 37°C for 2 hr. PCR conditions were essentially the same as in the genomic PCR described above except the annealing temperature was changed from 56°C to 64°C, and the extension time was changed from 30 s to 5 min. PCR products were purified using QIAquick PCR purification Kit (Qiagen) and sequenced. Mutations were detected by direct sequencing. The GenBank accession numbers are as follows: *ift88*, AY491507; *ift57*, AY600454; *ift52*, AY600455; *ift20*, AY600453.

Morpholino Knockdown and Phenotypic Rescue

Morpholino oligonucleotide knockdowns were performed as described previously (Malicki et al., 2002). For each gene, we used a morpholino targeted to the 5′ untranslated region (ATG Morpholinos) and an anti-splice site morpholino (SP Morpholinos). The efficiency of SP morpholino knockdown was determined by RT-PCR analysis as above. The following morpholinos were used: *ift88*ATG, GCC TTATTAAACAGAAATACTCCCA; *ift88*SP, CAACTCCACTCACCCCA TAAGCTGT; *ift52*ATG, ATTTCTTTGCTCTTTGTCCATGCTG; *ift52*SP, TAGCTTCACCTCAGCAGCAGTGAAC; *ift57*ATG, CCTCCATCAACA CGAACATCTGATA; *ift57*SP, GTTATCGCCTCACCAGGGTTCGAAG; *ift140*ATG, TCGGTGATCAAAATACACAGCCATG); *ift140*SP, AGT GATCATGTCTTACCTGCTGCAG. The *ift140*SP morpholino knockdown resulted in the insertion of the following sequence (capitalized, stop codons underlined): atctttacctgcagcAGGTAAGACATGATCAC TGTAATATATATTGGGagggtgaacat. Two morpholinos, one directed to *ift88* and one to *ift57* 5′ untranslated regions, caused severe developmental delays and were not used for further experiments. To test whether the ovl^{tz288b} allele is amorphic, morpholinos were injected into F2 diploid embryos obtained by in-crossing F1 mapping animals. *ovl* mutant homozygotes were identified by genotyping the MTJM10RFLP polymorphism as above.

To rescue the *ovl* phenotype, full-length *ift88* coding sequence was amplified by RT-PCR and cloned into the pXT7 vector (Figure 1 in Malicki et al., 2002). The resulting construct was linearized and served as a template in a transcription reaction using the mMessage mMachine kit (Ambion). Approximately 40 pg of RNA was injected into embryos at 1-cell stage.

Histology

For histological analysis, embryos were fixed in 4% paraformaldehyde (PFA, w/v, pH 7.4) in PBST overnight at 4°C. Embedding, sectioning, and staining were performed as described previously (Malicki, 1999; Pujic and Malicki, 2001).

Immunohistochemistry and Immunoblotting

Antibody staining was performed on whole animals or on frozen sections as described in previous publications (Malicki, 1999; Pujic and Malicki, 2001). The following primary antibodies and dilutions were used: mouse anti-acetylated α-tubulin (1:500, Sigma); mouse (1:200, Sigma) or rabbit (1:200, Sigma) anti-γ-tubulin; Zpr-1 (1:200, Oregon Monoclonal Bank); rabbit anti-rodopsin (1:5000, gift from D.R. Hyde); and rabbit anti-IFT88 (1:200, gift form J.G. Pazour). For IFT staining, prior to blocking, slides were immersed in 10% sodium citrate for 10 min at 90°C and washed in PBST (3 times, 5 min each). In whole-mount labeling experiments, embryos were blocked in 10% goat serum, 0.5% Triton X-100 in PBST for 2 hr, and incubated overnight in the presence of mouse monoclonal anti-acetylated-α-tubulin antibody (1:500, clone 6-11B-1, Sigma). To visualize F-actin, rhodamine-conjugated phalloidin (1:40, Molecular Probes) was added to the secondary antibody solution. Following washes, embryos were embedded in 1% low melting point agarose and viewed by confocal microscopy using the Leica HCX APO L40X lens.

For immunoblotting, embryos were homogenized in Laemmli loading buffer at 1 embryo/5 μl of buffer. Following the measurement of protein concentration using BCA Protein Assay Reagent (Pierce), the homogenate containing 20 μg of protein was separated using conventional SDS-PAGE, transferred to the PVDF membrane, and blocked as described in instructions to Immun-Star Chemiluminescent Protein Detection Systems (Bio-Rad). Membranes were incubated with rabbit anti-Ift88 antibody (1:150) or rabbit anti-rodopsin antibody (1:2000), washed, and developed according to detection kit manufacturer's directions (Bio-Rad).

In Situ Hybridization

The entire coding region of the zebrafish *omp* gene was amplified by RT-PCR using ATGCTCCTGGAGTTGACGTTC and TCACTTGGA GGTCTGGAATTCA primers and cloned into pZero-1 vector (Invitrogen). Hybridization, washes, and signal detections were carried out using standard protocols (Malicki, 1999; Pujic and Malicki, 2001).

DiI Labeling

Approximately 60 mg of NeuroTrace DiI tissue labeling paste (Molecular Probes) was dissolved in 700 μl of DMSO and diluted with 1% ethanol in egg water to the final volume of 10 ml. Living embryos were incubated in this solution for 10 min at 4 dpf, washed twice in egg water, embedded in 1% low melting point agarose, and viewed using a confocal microscope as above.

Evaluation of Light Damage

Embryos were reared on a light cycle of 14 hr of light exposure (350 Lux) and 10 hr of darkness (0 Lux) at 28°C until 48 hpf and subsequently subdivided into 3 groups that were treated with the following light exposure regimen: constant light of 750 Lux; constant darkness (0 Lux); and the light/dark cycle as above. In a separate experiment, the constant darkness group was subdivided into two:

one batch of embryos remained in constant darkness until 108 hpf, while the second was exposed to light of 750 Lux from 96 hpf to 108 hpf. Embryos were collected at appropriate time points, fixed, cryosectioned, and stained with anti-rod opsin and Zpr-1 antibodies as above. Light intensity was measured using Model 401025 digital light meter (Extech Instruments). A nonpaired t test was performed to determine the statistical significance of cell number changes.

Other Protocols

Apoptotic cell death was detected using the In Situ Cell Death Detection Kit (Roche) as described previously (Pujic and Malicki, 2001). For ultrastructural analysis, embryos were fixed in 4% (w/v) paraformaldehyde/2% glutaraldehyde in 75 mM phosphate buffer (pH 7.2) overnight at 4°C, postfixed with 2% osmium tetroxide in 50 mM phosphate buffer (pH 7.2). Subsequent steps were performed according to standard protocols (Malicki, 1999).

Acknowledgments

We thank Drs. Greg Pazour and Joseph Besharse for an anti-IFT88 antibody, Dr. Jim Fadool for the rod opsin-GFP transgenic zebrafish line, Dr. Ed Mroz for advice regarding statistical analysis, and Norman Michaud for expert help with electron microscopy. Drs. Francesca Pignoni, Bill Sewell, and Bill Campbell provided many helpful comments on the previous versions of this manuscript. These studies were supported by a Knights Templar Pediatric Ophthalmology research grant (to M.T.), the NIDCD grant R01DC005103 (to J.M.), and the NEI grant R01EY11882 (to J.M.).

Received: December 3, 2003
Revised: March 17, 2004
Accepted: April 24, 2004
Published: June 9, 2004

References

Alfinito, P.D., and Townes-Anderson, E. (2002). Activation of mislocalized opsin kills rod cells: a novel mechanism for rod cell death in retinal disease. Proc. Natl. Acad. Sci. USA *99*, 5655–5660.

Brand, M., Heisenberg, C.P., Warga, R.M., Pelegri, F., Karlstrom, R.O., Beuchle, D., Picker, A., Jiang, Y.J., Furutani-Seiki, M., van Eeden, F.J., et al. (1996). Mutations affecting development of the midline and general body shape during zebrafish embryogenesis. Development *123*, 129–142.

Cole, D.G., Diener, D.R., Himelblau, A.L., Beech, P.L., Fuster, J.C., and Rosenbaum, J.L. (1998). Chlamydomonas kinesin-II-dependent intraflagellar transport (IFT): IFT particles contain proteins required for ciliary assembly in *Caenorhabditis elegans* sensory neurons. J. Cell Biol. *141*, 993–1008.

Doerre, G., and Malicki, J. (2002). Genetic analysis of photoreceptor cell development in the zebrafish retina. Mech. Dev. *110*, 125–138.

Dynes, J.L., and Ngai, J. (1998). Pathfinding of olfactory neuron axons to stereotyped glomerular targets revealed by dynamic imaging in living zebrafish embryos. Neuron *20*, 1081–1091.

Fadool, J.M. (2003). Development of a rod photoreceptor mosaic revealed in transgenic zebrafish. Dev. Biol. *258*, 277–290.

Ghadami, M., Tomita, H.A., Najafi, M.T., Damavandi, E., Farahvash, M.S., Yamada, K., Majidzadeh, A.K., and Niikawa, N. (2000). Bardet-Biedl syndrome type 3 in an Iranian family: clinical study and confirmation of disease localization. Am. J. Med. Genet. *94*, 433–437.

Green, J.S., Parfrey, P.S., Harnett, J.D., Farid, N.R., Cramer, B.C., Johnson, G., Heath, O., McManamon, P.J., O'Leary, E., and Pryse-Phillips, W. (1989). The cardinal manifestations of Bardet-Biedl syndrome, a form of Laurence-Moon-Biedl syndrome. N. Engl. J. Med. *321*, 1002–1009.

Haddon, C., and Lewis, J. (1996). Early ear development in the embryo of the zebrafish, *Danio rerio*. J. Comp. Neurol. *365*, 113–128.

Han, Y.G., Kwok, B.H., and Kernan, M.J. (2003). Intraflagellar transport is required in *Drosophila* to differentiate sensory cilia but not sperm. Curr. Biol. *13*, 1679–1686.

Hansen, A., and Zeiske, E. (1993). Development of the olfactory organ in the zebrafish, *Brachydanio rerio*. J. Comp. Neurol. *333*, 289–300.

Haycraft, C.J., Swoboda, P., Taulman, P.D., Thomas, J.H., and Yoder, B.K. (2001). The *C. elegans* homolog of the murine cystic kidney disease gene Tg737 functions in a ciliogenic pathway and is disrupted in osm-5 mutant worms. Development *128*, 1493–1505.

Hudspeth, A.J., and Jacobs, R. (1979). Stereocilia mediate transduction in vertebrate hair cells (auditory system/cilium/vestibular system). Proc. Natl. Acad. Sci. USA *76*, 1506–1509.

Kernan, M., Cowan, D., and Zuker, C. (1994). Genetic dissection of mechanosensory transduction: mechanoreception-defective mutations of *Drosophila*. Neuron *12*, 1195–1206.

Kimmel, C.B., Ballard, W.W., Kimmel, S.R., Ullmann, B., and Schilling, T.F. (1995). Stages of embryonic development of the zebrafish. Dev. Dyn. *203*, 253–310.

Leinders-Zufall, T., Rand, M.N., Shepherd, G.M., Greer, C.A., and Zufall, F. (1997). Calcium entry through cyclic nucleotide-gated channels in individual cilia of olfactory receptor cells: spatiotemporal dynamics. J. Neurosci. *17*, 4136–4148.

Makino, C.L., Wen, X.H., and Lem, J. (2003). Piecing together the timetable for visual transduction with transgenic animals. Curr. Opin. Neurobiol. *13*, 404–412.

Malicki, J. (1999). Development of the retina. Methods Cell Biol. *59*, 273–299.

Malicki, J., Neuhauss, S.C., Schier, A.F., Solnica-Krezel, L., Stemple, D.L., Stainier, D.Y., Abdelilah, S., Zwartkruis, F., Rangini, Z., and Driever, W. (1996). Mutations affecting development of the zebrafish retina. Development *123*, 263–273.

Malicki, J., Jo, H., Wei, X., Hsiung, M., and Pujic, Z. (2002). Analysis of gene function in the zebrafish retina. Methods *28*, 427–438.

Meyer, M., Wilson, P., and Schomburg, D. (1996). Hydrogen bonding and molecular surface shape complementarity as a basis for protein docking. J. Mol. Biol. *264*, 199–210.

Moyer, J.H., Lee-Tischler, M.J., Kwon, H.Y., Schrick, J.J., Avner, E.D., Sweeney, W.E., Godfrey, V.L., Cacheiro, N.L., Wilkinson, J.E., and Woychik, R.P. (1994). Candidate gene associated with a mutation causing recessive polycystic kidney disease in mice. Science *264*, 1329–1333.

Murcia, N.S., Richards, W.G., Yoder, B.K., Mucenski, M.L., Dunlap, J.R., and Woychik, R.P. (2000). The Oak Ridge Polycystic Kidney (orpk) disease gene is required for left-right axis determination. Development *127*, 2347–2355.

Pazour, G.J., Dickert, B.L., Vucica, Y., Seeley, E.S., Rosenbaum, J.L., Witman, G.B., and Cole, D.G. (2000). *Chlamydomonas* IFT88 and its mouse homologue, polycystic kidney disease gene tg737, are required for assembly of cilia and flagella. J. Cell Biol. *151*, 709–718.

Pazour, G.J., Baker, S.A., Deane, J.A., Cole, D.G., Dickert, B.L., Rosenbaum, J.L., Witman, G.B., and Besharse, J.C. (2002). The intraflagellar transport protein, IFT88, is essential for vertebrate photoreceptor assembly and maintenance. J. Cell Biol. *157*, 103–113.

Perkins, L.A., Hedgecock, E.M., Thomson, J.N., and Culotti, J.G. (1986). Mutant sensory cilia in the nematode *Caenorhabditis elegans*. Dev. Biol. *117*, 456–487.

Pugh, E., and Lamb, T. (2000). Phototransduction in vertebrate rods and cones: molecular mechanisms of amplification, recovery, and light adaptation. In Handbook of Biological Physics, W. Stavenga, W. DeGrip, and E. Pugh, eds. (Amsterdam: Elsevier Science), pp. 183–255.

Pujic, Z., and Malicki, J. (2001). Mutation of the zebrafish glass onion locus causes early cell-nonautonomous loss of neuroepithelial integrity followed by severe neuronal patterning defects in the retina. Dev. Biol. *234*, 454–469.

Qin, H., Rosenbaum, J.L., and Barr, M.M. (2001). An autosomal recessive polycystic kidney disease gene homolog is involved in intraflagellar transport in *C. elegans* ciliated sensory neurons. Curr. Biol. *11*, 457–461.

Riley, B.B., Zhu, C., Janetopoulos, C., and Aufderheide, K.J. (1997). A critical period of ear development controlled by distinct populations of ciliated cells in the zebrafish. Dev. Biol. *191*, 191–201.

Rosenbaum, J.L., and Witman, G.B. (2002). Intraflagellar transport. Nat. Rev. Mol. Cell Biol. *3*, 813–825.

Rosenbaum, J.L., Cole, D.G., and Diener, D.R. (1999). Intraflagellar transport: the eyes have it. J. Cell Biol. *144*, 385–388.

Schrick, J.J., Onuchic, L.F., Reeders, S.T., Korenberg, J., Chen, X.N., Moyer, J.H., Wilkinson, J.E., and Woychik, R.P. (1995). Characterization of the human homologue of the mouse Tg737 candidate polycystic kidney disease gene. Hum. Mol. Genet. *4*, 559–567.

Sobkowicz, H.M., Slapnick, S.M., and August, B.K. (1995). The kinocilium of auditory hair cells and evidence for its morphogenetic role during the regeneration of stereocilia and cuticular plates. J. Neurocytol. *24*, 633–653.

Streisinger, G., Singer, F., Walker, C., Knauber, D., and Dower, N. (1986). Segregation analyses and gene-centromere distances in zebrafish. Genetics *112*, 311–319.

Tan, E., Wang, Q., Quiambao, A.B., Xu, X., Qtaishat, N.M., Peachey, N.S., Lem, J., Fliesler, S.J., Pepperberg, D.R., Naash, M.I., and Al-Ubaidi, M.R. (2001). The relationship between opsin overexpression and photoreceptor degeneration. Invest. Ophthalmol. Vis. Sci. *42*, 589–600.

Thompson, J.D., Higgins, D.G., and Gibson, T.J. (1994). CLUSTAL W: improving the sensitivity of progressive multiple sequence alignment through sequence weighting, position-specific gap penalties and weight matrix choice. Nucleic Acids Res. *22*, 4673–4680.

Yoshida, T., Ito, A., Matsuda, N., and Mishina, M. (2002). Regulation by protein kinase A switching of axonal pathfinding of zebrafish olfactory sensory neurons through the olfactory placode-olfactory bulb boundary. J. Neurosci. *22*, 4964–4972.

Zufall, F., and Leinders-Zufall, T. (2000). The cellular and molecular basis of odor adaptation. Chem. Senses *25*, 473–481.

9. 超音波とマイクロバブルを用いたラット網膜への遺伝子導入

園田祥三、内野英輔、坂本泰二
（鹿児島大）

研究要旨　すでに臨床応用されている超音波やマイクロバブル(以下MB)を組み合わせた新しい遺伝子導入法(ソノポレーション)について、眼球での効果および安全性について検討した。実験はラット網膜をターゲットにルシフェラーゼアッセイを用いて遺伝子導入効率を検討した。先に検討した角膜と異なり、網膜では超音波及びMBを併用した場合、遺伝子導入が可能であった。超音波条件；2w/cm²,duty cycle50%, 240秒で最が効率よく導入可能で、組織障害も認めなかった。ソノポレーションの眼球への利用の可能性が期待できる。

A．研究目的

超音波エネルギーを利用した薬物治療や遺伝子導入法が注目を集めている。そのメカニズムは、主に超音波照射時に発生する小さな泡によるキャビテーション効果によって細胞膜の構造が変化して膜透過性亢進し、細胞周囲の物質が効率的に取り込まれると考えられている。マイクロバブル(以下 MBと略す)を併用すると、細胞への物質の取り込みがさらに増加することも分かっている。MBとは内部にガスを持つマイクロサイズの泡の事である。我々は、この方法をつかって角膜に遺伝子導入が可能であることを証明してきた。今回、*in vivo* で超音波による網膜への遺伝子導入が可能か検討した。

B．研究方法

ウィスターラット硝子体腔に33G針でルシフェラーゼプラスミドを10μl注射し、超音波照射装置（ソニトロン 2000™）を使用して角膜から各種条件で超音波を照射した。さらにMB（オプチゾン™）を付加し同様の実験を行った。眼球摘出後、網膜をホモジナイズし、ルシフェラーゼアッセイによって注射単独群・超音波照射群・超音波とMB併用群での遺伝子導入効率を判定した。また、網膜への遺伝子導入部位を調べるために、抗ルシフェラーゼ抗体による免疫染色を行った。サーモグラフィーやH.E.染色による組織への安全性についても併せて検討した。

（倫理面への配慮）

動物実験は、鹿児島大学動物実験倫理規定に従って実験を行った。

C．研究結果

プラスミド硝子体注射群、超音波照射群でも軽度網膜に遺伝子導入された。超音波照射（1mHz, 2w/cm²,duty cycle50%, 240秒）にMBを併用群が最も高率に遺伝子導入された(図, scheffe' s test $p<0.05$)。免疫染色では、プラスミド単独群、超音波照射群ではほとんど陽性所見はなかったが、MB 併用群では網膜神経節繊維層、内顆粒層の硝子体腔に近い層に多くの陽性所見を認めた。

また、検討を行った超音波条件では、組織学的には明らかな異常はなかった。サーモグラフィーでは、超音波照射部の温度は 37 度を超えることはなかった。

図

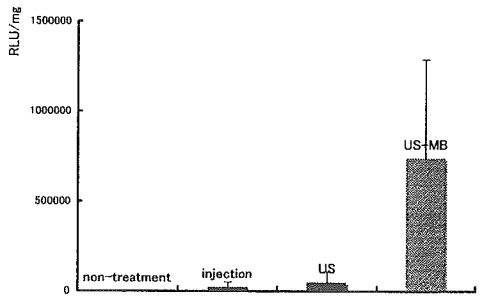

投与法の違いによる網膜への luciferase 導入効果

D. 考察

網膜の硝子体腔に近い層に強く遺伝子導入されていたこと、MB 併用群が有意に導入効率が高かったことから、超音波エネルギーと MB を併用することによって、初めて網膜のバリア機能を可逆的に変化させ、網膜へ遺伝子が取り込まれた可能性が高い。

E. 結論

超音波照射および MB によってラット網膜へ遺伝子導入が可能であった。超音波や MB を利用した、新たな網膜への遺伝子導入の開発につながる可能性がある。

F. 健康危険情報

なし

G. 研究発表

1. 論文発表

1. Shozo Sonoda et al : Gene transfer to corneal epithelium and keratocyte mediated by ultrasound with microbubbles, IOVS in press.

2. 学会発表

1. 園田祥三　他：ソノポレーション法による角膜への遺伝子導入、第 2 回超音波薬物・遺伝子導入研究会. 福岡、2005
2. 園田祥三：超音波とマイクロバブルを用いたドラッグデリバリーシステム. 第 59 回日本臨床眼科学会、シンポジウムドラッグデリバリー、札幌、2005
3. 園田祥三 他：眼瞼メラノーマに対する超音波とマイクロバブル併用時のブレオマイシンの抗腫瘍効果の検討. 第 2 回 ソノポレーション研究会、福岡、2006

H. 知的財産権の出願・登録状況

1. 特許取得(出願中)

眼球組織への生理活性薬剤導入のための組成物および装置。

出願番号　特許 2005-221346

2. 実用新案登録

なし

3. その他

なし

I. 参考文献

1. Tachibana K et al: Induction of cell-membrane porosity by ultrasound. Lancet. 353: 1409, 1999.
2. Sakamoto T et al: Target gene transfer of tissue plasminogen activator to cornea by electric pulse inhibits intracameral fibrin formation

and corneal cloudiness. Hum Gene Ther. 10: 2551-2557, 1999.
3. Taniyama Y et al: Development of safe and efficient novel nonviral gene transfer using ultrasound: enhancement of transfection efficiency of naked plasmid DNA in skeletal muscle. Gene Ther. 9: 372-380, 2002.
4. Marshall E: Gene therapy's growing pains.Science. 269 :1050,1052-1055, 1995.
5. Shozo Sonoda et al: Gene transfer to corneal epithelium and keratocyte mediated by ultrasound with microbubbles, IOVS in press

10. Wrapped Liposome siRNAの
マウス脈絡膜新生血管モデルにおける動態検討

高橋秀徳[1)]、小畑　亮[2)]、柳　靖雄[1)]、玉置泰裕[1)]
真鍋一郎[3)]、八木信宏[4)]、山内雅博[4)]、永井良三[3)]
([1)] 東京大、[2)] さいたま赤十字、[3)] 東京大循環器内科、[4)] 協和発酵工業)

研究要旨　Wrapped Liposome は陽イオン性脂質二重層から成るコアと表面をポリエチレングリコールとする中性脂質二重層によっておおわれた si(small interfering) RNA/トランスフェクション試薬複合物から構成される。平均直径は 100nm でマウス血漿内半減期が長く、マウス腫瘍モデルにおいて高い集積性が確認されている。
今回我々はマウス脈絡膜新生血管 (CNV) モデルを用いて Wrapped Liposome siRNA 全身投与時の動態について検討した。また、血管新生関連因子を target とする siRNA を検討した。21 塩基対・ランダム配列の FAM siRNA を Wrapped Liposome に内包した。C57Bl/6J マウス(10-12 週齢)の右眼眼底に半導体レーザー(スポットサイズ 200μm、照射時間 0.02 秒、出力 200mW)を 3 箇所照射し, CNV モデルを作成した。レーザー照射 3 日後に Wrapped Liposome siRNA を静注し、2, 4, 8, 24 時間後, 2, 3, 4, 5, 6, 7, 日後に蛍光眼底撮影を行った。また、VEGFa, HIF-1 を target とする siRNA を合成し、C2C12 細胞に transfection し、3 日後に RT-PCR を行った。蛍光は静注 2 時間後から観察され、静注 8 時間後に蛍光が最大となり、1 週間後にも蛍光が観察された。また、VEGFa, HIF-1 は siRNA により knock down された。Wrapped Liposome siRNA は全身投与により CNV に高い集積性を示し、CNV 治療に有用である可能性が示唆された。

A. 研究目的

ナノ粒子を全身投与すると EPR (Enhanced Permeability and Retention) 効果により脈絡膜新生血管(CNV)への集積が見られるが、薬剤内包可能ナノ粒子の CNV 集積を検討している報告は少ない。我々は薬剤内包可能高分子ミセルの CNV 集積と抑制効果を発表しているが、今回我々は siRNA 内包可能な新規リポソーム製剤 Wrapped Liposome を用いて、CNV への集積を検討するとともに、siRNA による血管新生関連因子の knock down を検討した。

B. 研究方法

C57Bl/6J マウス(10-12 週齢)を用い、半導体レーザー808nm、スポットサイズ:200μm、照射時間：0.02 秒、出力：200mW で右眼眼底 3 箇所に CNV を作成し、照射 3 日後 Wrapped Liposome siRN を静注し、2 時間～7 日後に蛍光眼底撮影を行い、蛍光強度を半定量した。
VEGFa, HIF-1 をターゲットとした siRNA を

合成し、Silencer siRNA construction kit Ambionを用いてC2C12細胞にtransfectionし、3日後にRT-PCRにて両発現を検討した。

（倫理面への配慮）

動物実験はARVO statementに基づき行った。

C．研究結果

眼底の蛍光は2時間後より検出され、8時間後に最大輝度に達し、1週間後にも観察された。また、作成したsiRNAによりVEGFa, HIF-1の発現がknock downされた。

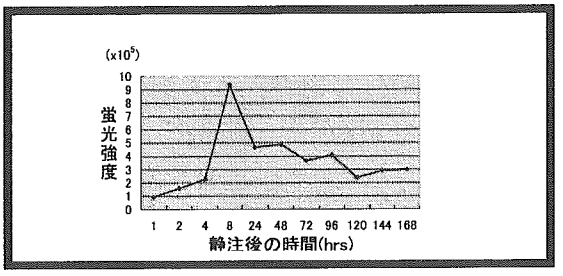

図1　蛍光強度の経時変化

D．考察

Wrapped Liposomeは既報の高分子ミセルと同様のEPR効果が認められ、またsiRNAの内包が容易であり、血漿中半減期も長い。また、siRNAによる血管新生関連因子のknock downが可能であったことから、Wrapped LiposomeはsiRNAを用いた治療に有用である可能性がある。

E．結論

Wrapped Liposome siRNAは全身投与によりCNVに高い集積性を示し、CNV治療に有用である可能性が示唆された。

F．健康危険情報

なし

G．研究発表

1．論文発表

1. Ideta R et al: Effective accumulation of polyion complex micelle to experimental choroidal neovascularization in rats. FEBS Lett 557(1-3): 21-25, 2004.
2. Ideta R,et al, Nanotechnology-based photodynamic therapy for neovascular disease using a supramolecular nanocarrier loaded with a dendritic photosensitizer. Nano Lett. 5(12): 2426-2431, 2005.

2．学会発表

1. Manabe I,et al, Luminal Flow Induces Calcium Oscillations In Cells Of The Cortical Thick Ascending Limb. American Heart Association, Dallas, Texas, 2005.

H．知的財産権の出願・登録状況

1．特許取得

出願済み

2．実用新案登録

なし

3．その他

なし

I．参考文献

1. Ysukawa T et al: Targeted delivery of anti-angiogenic agent TNP-470 using water-soluble polymer in the treatment of choroidal neovascularization. Invest Ophthalmol Vis Sci. 40(11):

2690-2696, 1999.
2. Ysukawa T et al: Targeting of interferon to choroidal neovascularization by use of dextran and metal coordination. Invest Ophthalmol Vis Sci. 43(3): 842-848, 2002.
3. Ideta R et al: Effective accumulation of polyion complex micelle to experimental choroidal neovascularization in rats. FEBS Lett 557(1-3): 21-25, 2004.
4. Mizumura Y et al, Cisplatin-incorporated polymeric micelles eliminate nephrotoxicity, while maintaining antitumor activity. Jpn J Cancer Res 92(3):328-336, 2001.
5. Fire A et al, Potent and specific genetic interference by double-stranded RNA in Caenorhabditis elegans. Nature 391(6669): 806-811, 1998.
6. Reich SJ et al, Small interfering RNA (siRNA) targeting VEGF effectively inhibits ocular neovascularization in a mouse model. Mol Vis 9: 210-216, 2003.
7. Tobe T et al, Targeted disruption of the FGF2 gene does not prevent choroidal neovascularization in a murine model. Am J Pathol 153(3): 1641-1646, 1998.
8. Ideta R,et al, Nanotechnology-based photodynamic therapy for neovascular disease using a supramolecular nanocarrier loaded with a dendritic photosensitizer. Nano Lett. 5(12): 2426-2431, 2005.